ADVANCED SUSTAINABLE SYSTEMS
www.advsustainsys.com

Visible-Light Photoreforming of Biomass Derivatives through MBi_2O_4-P25 Heterostructures: Study of the Influence of Metals (M = Cu, Ni, Zn, Co)

Muhammad Umair, Ahmed Malek Djaballah, Marianna Bellardita, Radia Bagtache, Leonardo Palmisano, and Mohamed Trari*

In this work, MBi_2O_4-P25 (M = Cu, Ni, Co, Zn) composites are successfully synthesized by a simple ball milling method by varying some parameters (rotation speed, rotation time, metal/TiO_2 ratio) to optimize the preparation conditions. The noble metal-free TiO_2-based photocatalysts are used to carry out the partial oxidation of glucose and glycerol with the simultaneous H_2 production under simulated solar light irradiation. Starting from glucose, 2.6 mmol of H_2 are obtained with a conversion of 34%, along with arabinose, formic acid and gluconic acid as main intermediates. By using glycerol, 3.2 mmol of H_2 are produced, with 17% conversion and the production of dihydroxyacetone and glycolic acid. The composites exhibit higher activity than pure P25 and $CuBi_2O_4$ (CBO). The produced H_2 amount is comparable to that reported in the literature by using Pt–TiO_2 photocatalysts. This study offers a paradigm for the future design of bifunctional photocatalysts for simultaneous noble metal-free H_2 production and biomass valorization under environmentally friendly conditions with a possible scale up of the process.

1. Introduction

Bioenergy deriving from biomass can be considered a clean and renewable energy alternative to that deriving from fossil resources.[1–3] Hydrogen has one of the highest energy capacities per unit mass and does not produce any pollutants during combustion.[4,5] For these reasons it is considered one of the most promising energy carriers, in particular when it is produced from a renewable energy source such as sunlight using also biomass derivatives.[6]

In the last years, heterogeneous photocatalysis has emerged as a very promising technique to respond to the environmental issues related to pollutants degradation and energy crisis, by fuel production and organic syntheses driven by solar light.[7–10] Pure water-splitting into O_2 and H_2 is not an easy process because of the large up-hill reaction and the rapid back reaction. Photoreforming, employing a sacrificial agent to consume holes, represents an up-hill process for H_2 production as energy demand is lower.[11,12] Notably, by photocatalytic reforming, the selective oxidation of cellulose-derived compounds, thus producing chemicals of high-added value, along with hydrogen is accomplished.[13–17] These include many different types of carboxylic acids, such as succinic, fumaric, malic, 2,5-furandicarboxylic, 3-hydroxypropionic, aspartic, glucaric, glutamic, glycolic, itaconic, and levulinic acids along with numerous other building-block molecules, such as 3-hydroxybutyrolactone, glycerol, fructose, glucose, and xylitol/arabinose.[7,18,19] Glucose and glycerol are two representatives of biomass whose valorisation is highly desirable. In particular, glucose is the most diffuse and cheapest carbohydrate as it can be directly obtained from cellulose, the most abundant and renewable biomass on Earth whilst glycerol is obtained in large amounts as a waste product of the biodiesel production industry. Valuable molecules as gluconic acid, arabinose and formic acid can be obtained starting from glucose,[14,20,21] while glyceraldehyde, dihydroxyacetone and glycolic acid are formed from glycerol.[22–24] Biomass derivatise have also been effectively employed to prepare derived carbon materials used as electrocatalysts for overall water splitting.[25,26]

Exploring efficient and scalable photocatalysts is a prerequisite for this purpose. In the past decades, numerous

M. Umair, M. Bellardita, L. Palmisano
Engineering Department
University of Palermo
Viale dell Scienze Ed. 6, Palermo 90128, Italy
E-mail: marianna.bellardita@unipa.it

A. M. Djaballah
Institute of Physical Chemistry
Polish Academy of Sciences
Kasprzaka 44/52, Warsaw 01-224, Poland

A. M. Djaballah, R. Bagtache
Laboratory of Electrochemistry-Corrosion
Metallurgy and Inorganic Chemistry
Faculty of Chemistry
USTHB
BP 32, Algiers 16111, Algeria

M. Trari
Laboratory of Storage and Valorisation of Renewable Energies
Faculty of Chemistry
USTHB
BP 32, Algiers 16111, Algeria

The ORCID identification number(s) for the author(s) of this article can be found under https://doi.org/10.1002/adsu.202400298

DOI: 10.1002/adsu.202400298

semiconductor photocatalysts have been reported, including, for instance, inorganic metal oxides/sulphides, transition metal layered double hydroxides, perovskite oxides, MOF compounds and polymer semiconductors.[16,27–34] Recently, the incorporation of other components to form coupled photocatalysts has been investigated to improve the photocatalytic performance for H_2 production due to their appropriate band gaps and catalytic activity.[16,35–38]

Among different semiconductors, titanium dioxide (TiO_2) has proven to be one of the most active and continues to attract much attention due to its low cost, non-toxicity, strong oxidizing power, excellent photocatalytic activity and long-term (photo)stability.[39,40] However, to achieve good H_2 production, some noble metals such as Ag and Pt have been generally used as co-catalysts combined with other oxides.[20,41–44] This limits its practical application due to high costs.

In the present investigation, to solve this problem, low-cost Cu, Ni, Co, Zn spinel oxide-based co-catalysts such as MBi_2O_4-P25 (M = Cu, Ni, Co, Zn) where P25 indicates the widely used commercial Aeroxide P25 TiO_2, have been studied to replace noble metals. The MBi_2O_4-P25 composites were characterized after their preparation by ball milling using different type and amount of the metal species, speed and rotation time. Furthermore, their photocatalytic performance was compared with that of bare P25 for H_2 production by photoreforming glucose and glycerol under green conditions. Ball milling is an effective, economical, simple and solvent-free technique for obtaining composite photocatalysts in large quantities, and therefore has a high potential, unlike other sophisticated methods, to also be applied industrially.[16,36,45,46]

2. Experimental Section

2.1. Materials

Copper(II) nitrate trihydrate $Cu(NO_3)_2{\cdot}3H_2O$ (Merck > 98%), bismuth(III) nitrate pentahydrate $Bi(NO_3)_3{\cdot}5H_2O$ (Merck > 98%), $Co(NO_3)_2{\cdot}3H_2O$ (Sigma-Aldrich), $Ni(NO_3)_2{\cdot}3H_2O$ (Sigma-Aldrich), $Zn(NO_3)_2{\cdot}3H_2O$ (Sigma-Aldrich), citric acid (Sigma-Aldrich), glucose (Sigma-Aldrich), arabinose (Sigma-Aldrich), gluconic acid (Sigma-Aldrich), formic acid (Sigma-Aldrich), KOH potassium hydroxide (Fluka 65%), glycerol (Sigma-Aldrich), glyceraldehyde, dihydroxyacetone, and glycolic acid were acquired from Merck, commercial TiO_2 P25 (Aeroxide) was purchased from Evonik Industries. All chemicals were used as received without further purification. Ultrapure deionized water was used throughout the study.

2.2. Photocatalysts Synthesis

2.2.1. Synthesis of MBi_2O_4 with M = Cu, Ni, Zn, Co

$CuBi_2O_4$ (CBO) was synthesized by a very facile co-precipitation method following the nitrate route. Cu $(NO_3)_2{\cdot}3H_2O$ and Bi $(NO_3)_3{\cdot}5H_2O$ were added in stoichiometric proportions to 50 ml distilled water. The mixture, after adjusting the pH at 12.20 with KOH, was air-heated at 140 °C for 48 h. The solid obtained was recovered by filtration, washed with water and dried at 60 °C. Our synthesis is different from that reported by many authors who used complexing agents in organic solvents and high temperature treatments.[47–50] $NiBi_2O_4$, $ZnBi_2O_4$, $CoBi_2O_4$, were synthesized by sol–gel route using $M(NO_3)_2{\cdot}3H_2O$ salts (M = Ni, Zn, Co) and Bi $(NO_3)_3{\cdot}5H_2O$ dissolved in stoichiometric proportions in water with a 5% excess of citric acid added. The solution was gradually evaporated on a hot plate and the amorphous powdered solid obtained was homogenized in an agate mortar and calcined at 800 °C in a programmed furnace (5 °C min^{-1}).

2.2.2. Synthesis of MBi_2O_4 -P25 Heterostructures

All the MBi_2O_4 heterosystems with different metals (M = Cu, Ni, Zn, Co) and P25 were obtained by mixing the two components in a planetary ball mill (PM 100, Retsch-Allee 1-5, 42 781 Haan, Germany) instrument. The combined powders were prepared by putting the powders inside a chrome steel jar coated with zirconium oxide filled with six zirconium oxide balls.

To optimize the synthesis conditions, $CuBi_2O_4$ -P25 composites were prepared at three different rotation speeds (100, 150 and 200 rpm) and rotation times (1, 2 and 3 h) in different weight ratios, such as 2, 3, and 4% of CBO with respect to P25. The codes used for the samples were X%MBO-P25@s rpm & th where X is the spinel percentage (2, 3, 4%), M the metal species (in particular, C = copper, N = nickel, Z = zinc and Co = cobalt), s the rotation speed (100, 150 or 200 rpm) and t the rotation time (1, 2 or 3 h).

2.3. Photocatalysts Characterization

The crystalline structure of all of the photocatalysts was investigated through X-ray diffraction (XRD) by a Philips X'Pert Pro diffractometer apparatus equipped with a Ni filtered Cu-Kα wavelength (λ = 1.54059, at a scan rate of 2° min^{-1} with the generator working at 45 kV and 40 mA. Raman spectra were recorded using a LabRam HRevolution Confocal micro-Raman spectrometer (Horiba Jobin Yvon) equipped with a 633 nm visible laser source (He-Ne) whose power was 17 mW. UV–Vis diffuse reflectance spectra were recorded from 190 to 800 nm with a Jasco 650 spectrophotometer equipped with an integrating sphere, and $BaSO_4$ was used as the reference. The photocatalysts were considered to be indirect semiconductors and the bandgap (E_g) values were calculated from the UV–vis DRS spectra using the Kubelka-Munk and Tauc Plot method. The specific surface areas (SSA) of the samples were determined by the single-point BET method using a Flow Sorb 2300 apparatus. The ATR-FTIR spectra were acquired by a Perkin Elmer FTIR spectrophotometer with a bandwidth of 2 cm^{-1}. The morphology of the powders was examined by scanning electron microscopy (SEM, with Schottky field emission (FESEM; JSM-JEOL). An XPS spectrometer, 250Xi/ESCALAB, Thermo-Fisher Scientific, USA, was used to obtain X-ray photoelectron spectra (XPS), by which the elementary chemical states of various elements were determined using Al-Kα radiation.

2.4. Photocatalytic Runs

The photocatalytic tests were carried out in a cylindrical 500 mL Pyrex batch photoreactor at room temperature and pressure with

glucose or glycerol as substrates. The runs were carried out at natural pH and the initial concentration was 1×10^{-3} M and 2×10^{-3} M for glucose and glycerol, respectively. The optimal quantity of catalyst was determined by measuring the photon flux transmitted after addition to water of increasing powder amounts by a Delta Ohm DO9721 radiometer; when the transmitted radiation was less than 10% with respect to the incident one (measured for pure water), catalyst addition was stopped.[51] The optimum quantity was 1.5 g L^{-1} for the CBO catalysts. For glucose a 150 W halogen lamp was used while for glycerol a 125 W medium pressure Hg lamp axially immersed inside the photoreactor, and the water circulating through a Pyrex thimble ensured that the temperature inside the reactor was maintained at approx. 303 K. A magnetic stirrer assured the suspension of the photocatalyst inside the reacting mixture. For both substrates the runs lasted 5 h.

The runs were carried out under anaerobic conditions: He was bubbled for 30 min under dark to achieve the adsorption-desorption equilibrium, then the reactor was sealed. Before adding the catalyst and switching on the lamp, the substrate concentration was measured to evaluate the extent of adsorption on the surface of catalysts. During irradiation, at specific intervals of time liquid samples were withdrawn and filtered through a 0.2 μm membrane to analyse glucose, glycerol and their degradation products.

The determination of concentration of glucose, glycerol and their derivatives over the irradiation time was performed using a Thermo Scientific Dionex UltiMate 3000 HPLC equipped with a DiodeArray and a refractive index detector. An aqueous solution of H_2SO_4 (2.5×10^{-3} M) at 0.6 mL^{-1} min was used as eluent for a REZEK ROA Organic acid H^+ column. For the quantification of the gaseous species (H_2 and CO_2) accumulated in the head space of the reactor, gas samples were withdrawn at various time intervals using a 500 μl syringe, and they were analysed through a HP 6890Series GC System equipped with a Supelco packed column GC60/80 Carboxen−1000 and a thermal conductivity detector. He was used as the carrier gas in the GC.

Conversion X, and selectivity to products S, were calculated by using the following equations:

$$X = \frac{C_{,i} - C_{,t}}{C_{,i}} \times 100 \quad (1)$$

$$S = \frac{P_{,t}}{C_{,i} - C_{,t}} \times 100 \quad (2)$$

where, $C_{,i}$ is the initial molar concentration, $C_{,t}$ the molar concentration at any time t and $P_{,t}$ the molar concentration of the product at any time t.[14]

3. Results and Discussion

3.1. Physico-Chemical Characterizations

The diffractograms of the different samples are reported in **Figure 1**. That of bare P25 displays both anatase and rutile characteristic peaks (anatase JCPDS NO. 99-0008, rutile JCPDS NO. 99-0090, respectively). The diffraction peaks related to the spinel

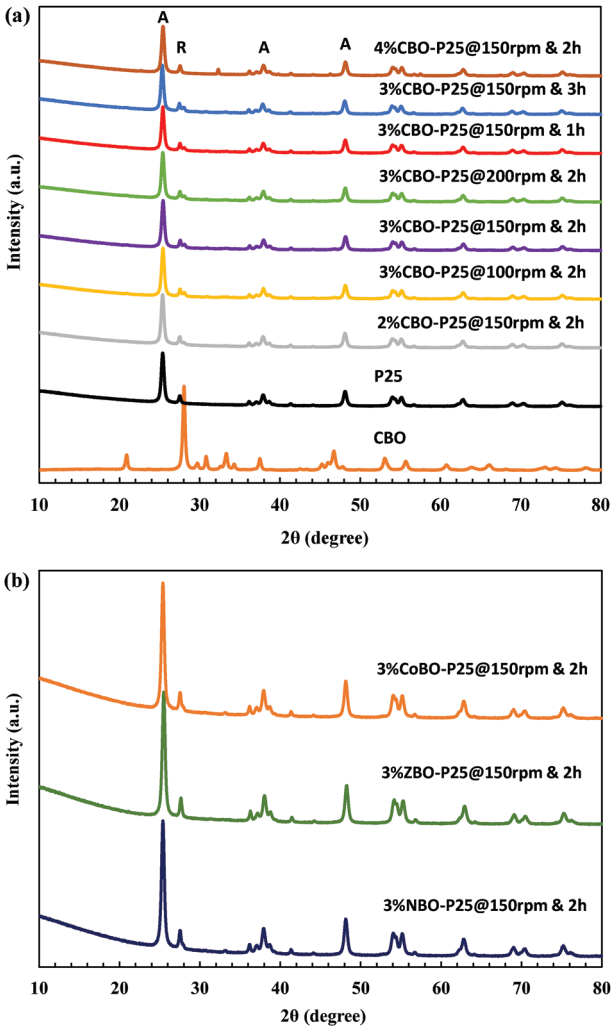

Figure 1. XRD patterns of a) CBO, P25, and CBO-P25 coupled samples prepared in different experimental conditions; b) MBO with M (Zn, Co and Ni)-P25 coupled samples. A = anatase and R = rutile.

ABi_2O_4 (A = Cu, Ni, Zn or Co) were not detected in the composites due to the low content of the latter in the heterosystems and its uniform dispersion in the TiO_2 matrix.

The size of nanocrystallites (D = 14.9 nm) was calculated by using the Williamson Hall equation (Equation 3, **Figure 2**) from the full width at half maxima (β) of the strongest TiO_2 peaks.[52] No substantial differences were noticed in the coupled samples.

$$\beta \cos\theta = k\lambda/D + 4\varepsilon \sin\theta \quad (3)$$

Raman spectroscopy was used to examine the structural characteristics of P25-based photocatalysts. The Raman spectrum of CBO (**Figure 3a**) shows seven active bands at 76, 122, 128, 186, 258, 400 and 581 cm^{-1}. The B_{2g} mode of the in-plane bending vibration of the Bi polyhedral is correlated with the peak at 76 cm^{-1}. The peaks at 122 and 128 cm^{-1} are attributed to the translational vibration of the CuO_4 plane along the Z axis with the A_{1g} mode.[53] The peak at 186 cm^{-1} corresponds to the E_g

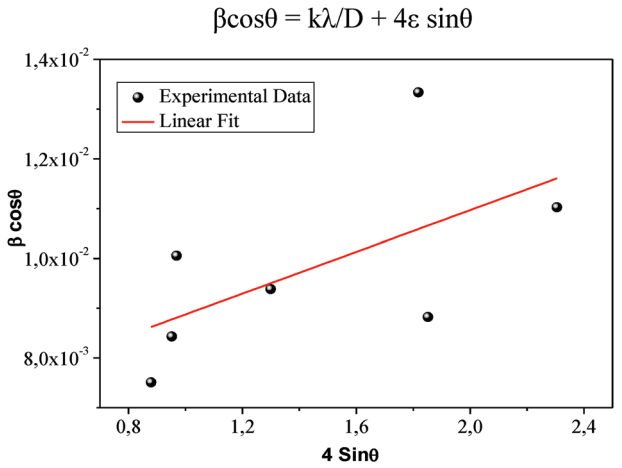

Figure 2. The crystallite size determined from the Williamson-Hall plot of 3% CBO-P25@150 rpm & 2 h.

mode of the Cu–Cu vibration, while the band at 258 cm^{-1} is attributed to the rotation of two CuO_4 squares stacked in opposite directions.[54] The band at 400 cm^{-1} highlights the A_{1g} mode of the Bi—O stretching vibration while the A_{1g} mode of the in-plane respiration of the CuO_4 squares is due to the band at 581 cm^{-1}. These observations are consistent with previous studies and support the tetragonal crystal structure of CBO. For P25-based photocatalysts (Figure 3b–d), a total of five characteristic Raman active modes with frequencies around 141, 193, 387, 505 and 626 cm^{-1} were obtained, belonging to the anatase Raman bands. No signal related to spinel oxides of Cu, Co, Ni can be observed (Figure 3d), due to their low quantity and high degree of dispersion on the TiO_2 surface according to the XRD results. The enlargement of the anatase main peak at ca. 144 cm^{-1} (inset Figure 3b–d) reveals a slight shift towards lower wavenumber in the coupled samples. By considering that this vibrational mode is related to the O—Ti—O vibration, probably the presence of spinels causes a bond distortion that is reflected in a shift of the band.

The optical characteristics of the photocatalysts were investigated by the UV–Vis diffuse reflectance spectra (DRS). In **Figure 4a**, the DRS of different samples are displayed. The commercial P25 has an absorption beginning at 350 nm, which corresponds to the typical band-gap of anatase-rutile mixture. Due to its brown colour and small bandgap, CBO exhibits an absorption edge in the visible range between 620 and 800 nm.

The coupled MBi_2O_4 with M (Cu, Co, Ni, Zn) and TiO_2 systems display an enhancement in light absorption capacity in the visible region which is maximum in the sample containing the highest CBO percentage. Notably, another absorption edge at about 600 nm can be noticed in the composite samples. In accordance with the literature, the presence of these two absorption edges is typical of the formation of a heterostructure between the spinel and TiO_2.[55] Formation of all heterosystems between MBi_2O_4 and TiO_2 is expected to improve the light absorption capacity in terms of the photoactivation role of MBi_2O_4 responsible for electron transfer to TiO_2.

The bandgap of samples was calculated from the Tauc plots (Figure 4b) according to the following equation:[52]

$$(\alpha h\nu)^{1/n} = K \times (h\nu - E_g) \quad (4)$$

where α, $h\nu$, and E_g are the absorption coefficient, the light energy of photon, and the bandgap, respectively. K is a proportionality constant, while the exponent n indicates the transition nature, and it is equal to 2 and 0.5 for indirect and direct transition, respectively.

Bandgap values of the used samples are reported in **Table 1**. P25 displays a band gap value of 3.17 eV, typical of an anatase–rutile mixture while bare CBO showed absorption of visible light and band gap of 1.88 eV. For the heterostructures, values are slightly lower than that of P25 indicating that the interaction with spinel does not substantially modify the electronic structure of TiO_2.

P25 presents a specific surface area (SSA) of 50 $m^2\ g^{-1}$ while that of bare CBO is very low (2 $m^2\ g^{-1}$). All the coupled samples showed almost the same values as bare P25 due the low spinel amounts. Moreover, variations of speed, CBO percentage and treatment time in ball milling do not influence the SSA values of the composites with respect to P25. 3%ZBO-P25 sample shows a slightly higher value of 62 $m^2\ g^{-1}$.

Figure 5 shows a sequence of FTIR spectra for P25, bare CBO and 3% CBO-P25@150 rpm & 2 h samples. The spectrum of P25 clearly shows four bands. The broad band centred around 3500 cm^{-1}, corresponding to the stretching vibration of the hydroxyl —OH groups of the P25 surface,[56] is the broadest one. The band at around 1630 cm^{-1} corresponds to HOH bending mode of undissociated water molecules adsorbed on TiO_2 surface[57,58]; the peak at 1243 cm^{-1} could be attributed to carboxyl groups derived from adventitious residual organic species.[59] The band at ca. 731 cm^{-1} might be ascribed to the antisymmetric Ti—O stretching mode of the Ti—O—Ti.[58] According to previous findings,[16] CBO exhibits two prominent peaks at 1386 and 554 cm^{-1} resulting from the stretching vibration of the Bi—O and Cu—O bonds, respectively.

X-ray photo spectroscopy was used to study the surface chemical composition and electronic core levels of the composite samples. The XPS survey spectrum of the sample 3%CBO-P25@150 rpm & 2 h (**Figure 6a**) confirms the presence of C, O, Cu and Ti in the CBO-P25 coupled samples and the results are consistent with EDS element distribution determinations. The C signal observed at 284.6 eV originates from the amorphous carbon applied to calibrate the binding energy scale.

Figure 6b shows high-resolution XPS analysis of the Ti 2p region. The two peaks at 458.13 and 463.83 eV correspond to $2p_{3/2}$ and $2p_{1/2}$ binding energies of Ti^{4+} arranged in the anatase tetragonal structure.[37,60] As shown in Figure 6c, the peaks at 529.23 and 529.93 eV are related to O 1s binding energies and indicate the existence of two chemical states of oxygen in all catalysts: crystal lattice oxygen and off-lattice oxygen surface hydroxyl groups, respectively. Additionally, the high binding energy peak at 532.7 eV can be ascribed to weakly adsorbed organic oxygen or to surface defects.[55,61] The Cu 2p central level spectrum is displayed in Figure 6d. The main peak at ca. 933 eV and the shake-up satellite peaks with higher binding

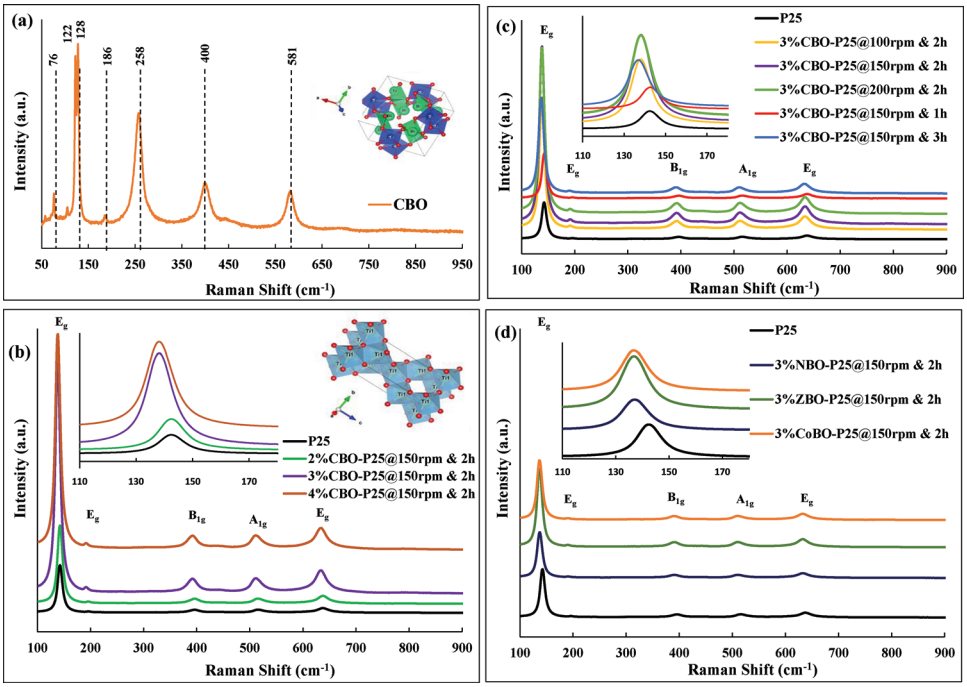

Figure 3. Raman spectra of the different samples.

energy (ca. 941 and 943 eV) are assigned to Cu^{2+}[62] whereas the peak at ca. 953.5 eV can be attributed to the binding energy of Cu^{+}.[63]

The morphology of the most active sample 3%CBO-P25@150 rpm & 2 h (**Tables** 2 and 3) was explored by SEM analysis (**Figure** 7). The distribution of the particles is uniform and irregular, and shaped agglomerates are present indicating a good mixing of the two components. The energy dispersion spectrum (EDS), in accordance with XPS measurements, confirms the presence of O, Ti, Cu and Bi (Figure 7a), and Cu and Bi

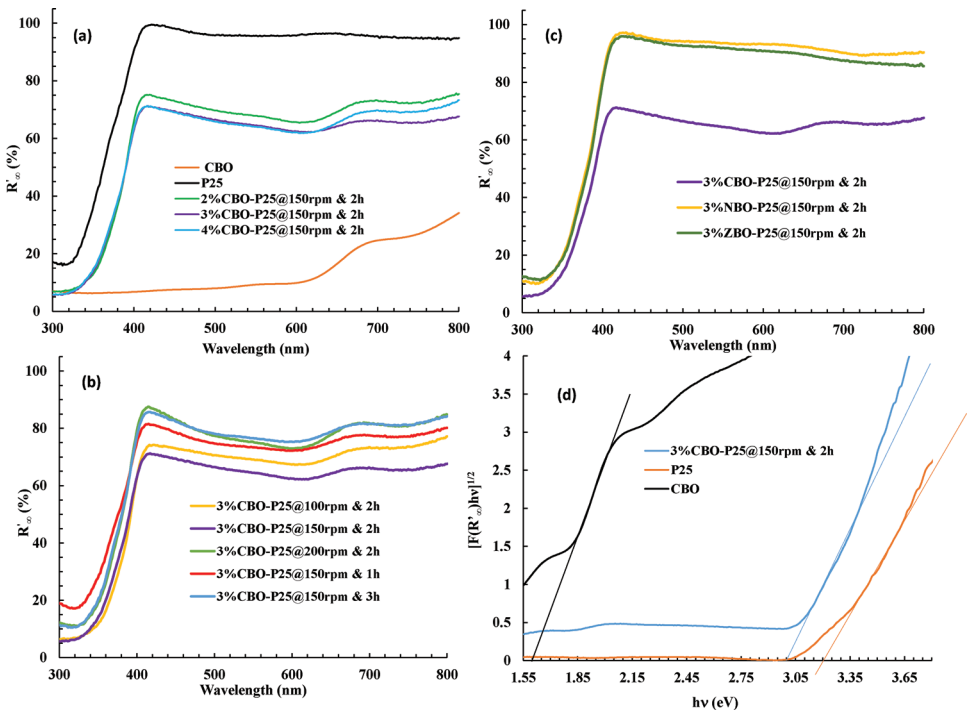

Figure 4. a–c) UV–Vis diffuse reflectance spectra of the different samples; d) bandgap energy calculation of P25, bare CBO, and the 3%CBO-P25@150 rpm & 2 h composite sample.

Table 1. S.S.A. and band gap values of the different samples.

Sample	S.S.A [m^2 g^{-1}]	Bandgap [eV]
P25	50	3.17
CBO	2	1.88
2%CBO-P25@150 rpm & 2h	53	3.10
3%CBO-P25@100 rpm & 2h	48	3.10
3%CBO-P25@150 rpm & 2h	46	3.05
3%CBO-P25@150 rpm & 1h	45	3.12
3%CBO-P25 @200 rpm & 2h	52	3.11
3%CBO-P25@150 rpm & 3h	49	3.12
4%CBO-P25@150 rpm & 2h	50	3.11
3%NBO-P25@150 rpm & 2h	45	3.12
3%CoBO-P25@150 rpm & 2h	46	3.13
3%ZBO-P25@150 rpm & 2h	62	3.12

are present in small amounts in the coupled systems. Furthermore, the EDS elemental mapping images (Figure 7b) reveal the homogeneous distribution of the different elements supporting the successful formation of a heterostructure between CBO and P25.

3.2. Photocatalytic Activity: Influence of Spinel Amount, Rotation Speed, Rotation Time, and Metal Species

MBi_2O_4-P25 photocatalysts containing different metal species were used for photoreforming of both glucose and glycerol substrates in aqueous solution. Concentrations of species formed in the liquid phase (arabinose, gluconic acid, formic acid, and gaseous phase (H_2 and CO_2) during partial oxidation of glucose versus irradiation time in the presence of selected catalysts are reported in **Figure 8**. **Figure 9** reports, instead, the concentrations of glyceraldehyde, dihydroxyacetone, glycolic acid and H_2 and CO_2 derived from glycerol. The concentration of the two substrates gradually decreases while that of the compounds deriving from their partial oxidation and of the products in the gaseous phase increases. P25 resulted in the formation of arabinose, gluconic acid and formic acid from glucose reforming while the products deriving from glycerol were dihydroxyacetone, glyceraldehyde and glycolic acid. For both substrates no H_2 was obtained in the presence of the bare P25 photocatalyst and CO_2, deriving from substrates mineralization, was formed only in low quantities. Bare CBO displayed a negligible activity both towards glucose and glycerol. The behaviour of the composite samples was like that of P25 giving rise to the same compounds but with a different distribution and higher conversion of the two substrates. The amount of converted glucose and fructose in the presence of the coupled systems is higher than that of bare P25 highlighting a more effective charges separation probably due to the formation of an effective heterojunction.[55] Notably, from perusal of Tables 2 and 3 can be observed that the two bare photocatalysts are inefficient for H_2 production whilst it is formed in the presence of the heterostructures. This finding is very interesting because the valuable energy carrier is produced without the addition of noble metal species as Pt. The optimization of preparation conditions (CBO percentages, different rotation speed and treatment time) allowed to enhance the efficiency both towards H_2 production and high value-added compounds formation.

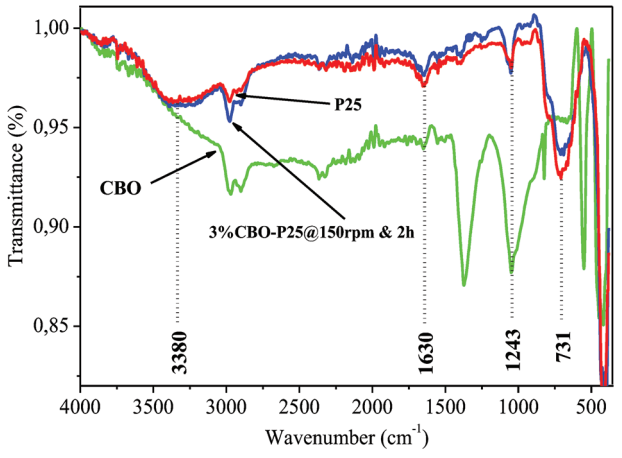

Figure 5. FTIR spectra of TiO_2, CBO, and 3%CBO-P25@150 rpm & 2 h.

To study how the rotation speed and time of ball milling treatment influence on the photoactivity, 3%CBO-P25 samples (the CBO percentage with respect to TiO_2 was chosen considering previous results[36,37]) were prepared by mixing the two components at three different ball milling rpm (Table 2 entries 3–5) for 2 h. By increasing the rotation speed from 100 to 150 rpm, 36% increasing in glucose conversion was noticed with the contemporary slight enhancement in the selectivity and a 73% increase in H_2 concentration. The further increase in speed to 200 rpm did not more increase the performance of the catalyst, obtaining almost the same conversion, a small increase in selectivity towards arabinose and a lower production of H_2. Probably at 150 rpm an optimal mixing of the two components can be obtained. Therefore, set the rotation speed at 150 rpm, 3%CBO-P25 heterostructures were prepared by varying the treatment time in the ball milling from 1 to 3 hours. The best samples resulted 3%CBO-P25@200 rpm & 2 h as 3%CBO-P25@200 rpm & 1 h and 3%CBO-P25@200 rpm & 3 h samples showed a lower glucose conversion (ca. 27%) and H_2 and CO_2 production. The same trend, although with different conversion, selectivity and H_2 production values, was obtained with glycerol (Table 3), confirming the importance of organic compound-catalyst interaction in addressing the activity. In fact, with glycerol, lower conversion and selectivity values but generally slightly higher H_2 amounts were formed. By varying the CBO amount the best value was found to be 3%. For glucose reforming, the catalysts named 2%CBO-P25@150 rpm & 2 h and 4%CBO-P25@150 rpm & 2 h showed conversion of 33 and 36%, respectively and the amount of H_2 was 0.81 and 1.1 mM, respectively. The sample 2%CBO-P25@150 rpm & 2 h produced more arabinose and formic acid. When glycerol was the substrate, the three catalysts prepared at 150 rpm for 2 h, showed almost the same conversion, higher selectivity with 2 and 4% of CBO and the highest H_2 amount with the 3%CBO-P25@150 rpm & 2 h sample.

The 3%CBO-P25@150 rpm & 2 h sample proved to be the most effective sample towards H_2 formation using both glucose and glycerol as substrates. In fact, in its presence, H_2 was produced in concentrations of 2.6×10^{-3} M starting from glucose and 3.21×10^{-3} M in the presence of glycerol. The addition of CBO to

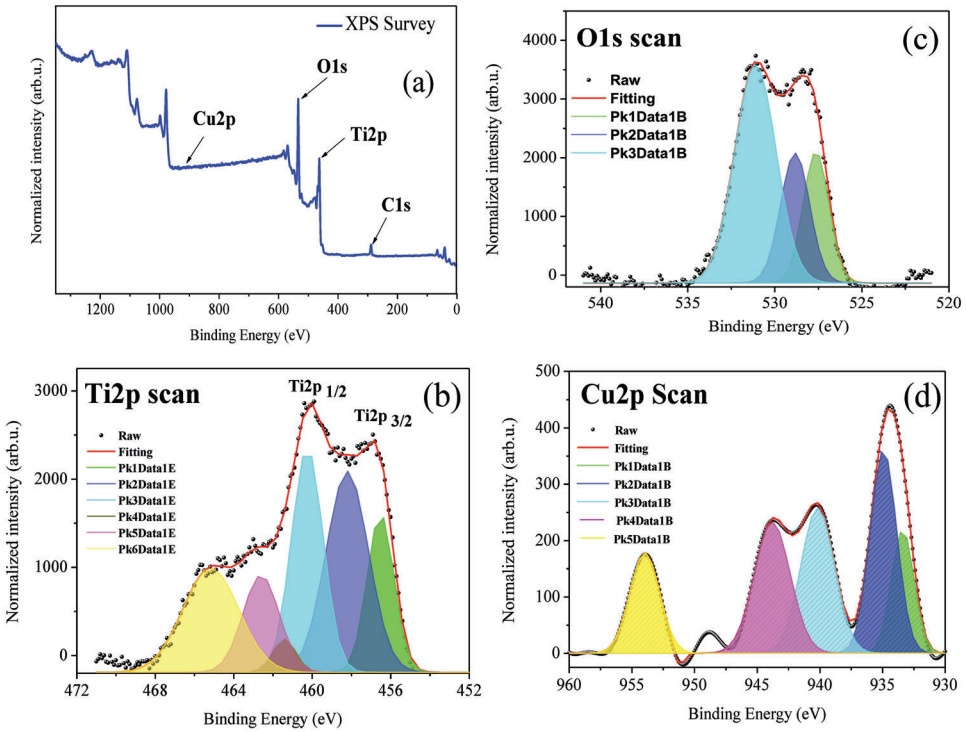

Figure 6. XPS spectra survey of a) 3%CBO-P25@150 rpm & 2 h and b) Ti 2p, c) O 1s, d) Cu 2p spectra.

P25 promoted the formation of an effective heterojunction enhancing both H_2 production and the formation of high-added value compounds and 3%CBO revealed to be the best combination. Higher amounts of CBO, probably prevent the TiO_2 surface from participating in the reactive process due to high surface coverage which causes poor light penetration.

To compare the effect of the presence of different metal species, some composites containing Ni, Co and Zn as metal species were prepared under the same conditions as the best 3%CBO-P25@150 rpm & 2 h photocatalyst, i.e., 150 rpm and 2 hours of milling, and their behaviour was compared with that sample for the photoreforming of glucose and glycerol.

All these composites afforded comparatively lower glucose conversion and H_2 and CO_2 amount than those containing CBO. No arabinose was found but the amount of gluconic acid was greater with the 3%CoBO-P25@150 rpm & 2 h. Among these composites, 3%ZBO-P25@150 rpm & 2 h showed high conversion and a significant amount of H_2, although the corresponding copper-containing composite performed better. It is not easy to fully explain why the presence of copper gives better results than other metals. It is known that the Cu^{2+}/Cu^{+} couple present in photocatalysts[36,64] such as TiO_2 and others, favours many oxidative and reductive processes (see for example the photoreduction of CO_2 and the oxidation of polluting organic molecules).[65] This

Table 2. Glucose conversion, selectivity towards different high value-added compounds and H_2 and CO_2 production.

Samples	X [%]	$S_{Arabinose}$ [%]	S_{GluA} [%]	S_{FA} [%]	H_2 [$\times 10^{-3}$ M]	CO_2 [$\times 10^{-3}$ M]
P25	19	46	6.7	32	–	0.02
CBO	4.7	–	–	–	–	negligible
3%CBO-P25@100 rpm & 2h	25	51	2.8	28	1.50	0.18
3%CBO-P25@150 rpm & 2h	34	57	2.3	32	2.60	0.19
3%CBO-P25@200 rpm & 2h	36	46	3.1	35	1.08	0.13
3%CBO-P25@150 pm & 1h	27	35	2.5	44	0.15	0.02
3%CBO-P25@150 rpm & 3h	26	48	2.4	46	0.12	0.04
2%CBO-P25@150 rpm & 2h	33	63	1.9	55	0.81	0.12
4%CBO-P25@150pm & 2h	36	45	2.0	43	1.10	0.14
3%NBO-P25@150 rpm & 2h	19	18	3.0	54	0.09	0.01
3%CoBO-P25@150 rpm & 2h	20	–	9.4	40	0.11	0.01
3%ZBO-P25@150 rpm & 2h	27	46	1.2	49	1.37	0.10

Table 3. Glycerol conversion, selectivity towards dihydroxyacetone and H_2 and CO_2 production.

Samples	X [%]	S_{GAld} [%]	S_{DHA} [%]	S_{GAcid} [%]	H_2 [× 10^{-3} M]	CO_2 [× 10^{-3} M]
P25	5	–	15.0	–	–	Negligible
CBO	5	–	–	–	–	Negligible
2%CBO-P25@150 rpm & 2h	15	23.3	23.5	30.5	1.57	0.07
3%CBO-P25@100 rpm & 2h	11	5.5	20.7	27.3	1.67	0.07
3%CBO-P25@150 rpm & 2h	17	4.9	13.2	17.2	3.21	0.09
3%CBO-P25@200 rpm & 2h	25	5.0	13.7	13.7	1.45	0.05
3%CBO-P25@150 rpm & 1h	23	4.4	17.1	11.3	1.32	0.04
3%CBO-P25@150 rpm & 3h	35	3.1	5.3	6.4	0.49	0.02
4%CBO-P25@150 rpm & 2h	16	6.2	20.3	28.0	1.17	0.04
3%ZBO-P25@150 rpm & 2h	29	3.3	6.1	12.4	1.34	0.05

work has indicated that even in more complex composite materials, it is likely that the versatility of copper to acquire electrons and lose them during irradiation facilitates some intermediate stages of the described reactions, the mechanism of which certainly deserves to be explored in more depth in subsequent works.

As for the reaction with glycerol, only the 3%ZBO-P25@150 rpm & 2 h sample was tested. The latter gave rise to a higher conversion (29% compared to 17%, with respect to the best copper-containing sample), i.e., 3%CBO-P25@150 rpm & 2 h, but less selectivity towards the major identified products and H_2 production.

In **Figure 10a** the hypothesized reaction pathway of glucose selective conversion is reported: the oxidation of the carbonyl to the carboxylic group led to the formation of gluconic acid, whilst the formation of arabinose occurs after breaking of the C1–C2 (α-scission) carbon bond with the contemporary formation of H_2 and HCOOH.[20,66] The main intermediates observed during glycerol conversion are 1,3 dihydroxyacetone, glyceraldehyde and glycolic acid. The first two compounds are formed by partial oxidation of the hydroxy group in position 1 or 2 to the carbonyl one, while the formation of glycolic acid arises from the C—C bond cleavage.[67]

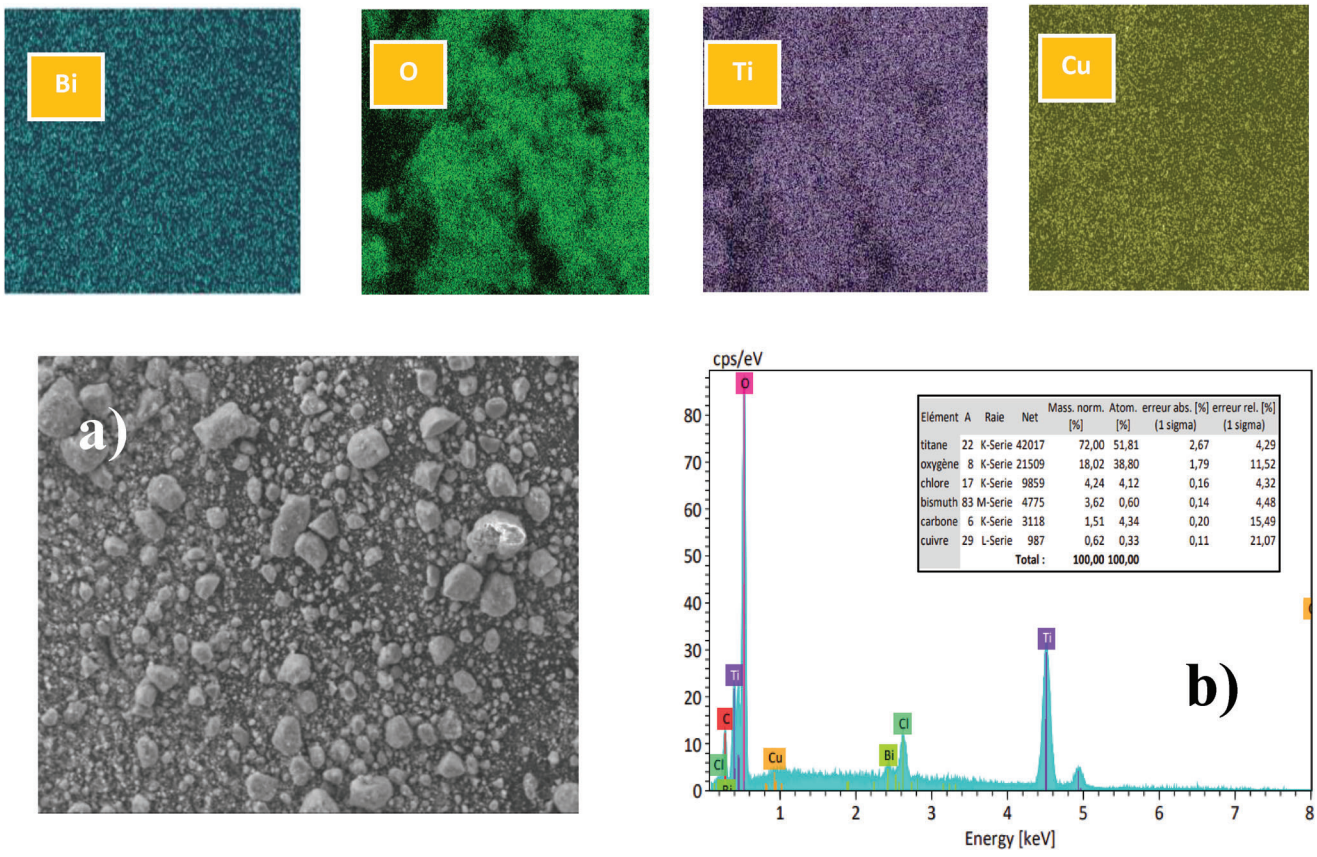

Figure 7. a) SEM image of 3% CBO-P25@150 rpm & 2 h; b) Mapping analysis using EDX.

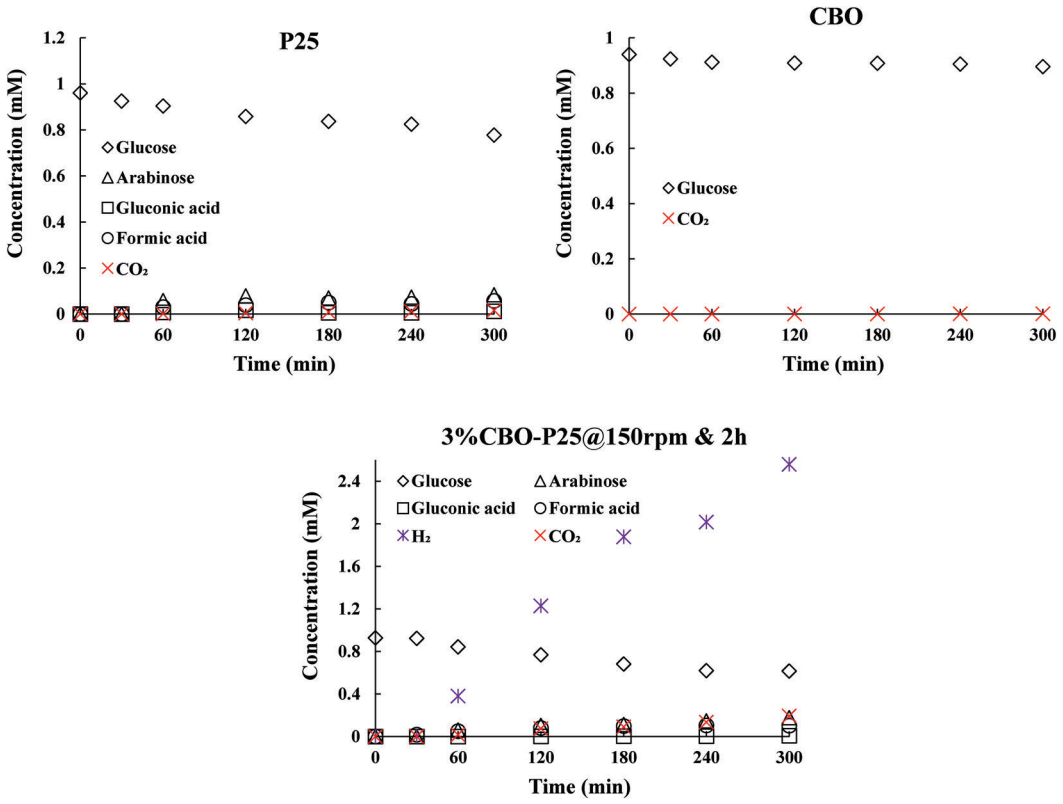

Figure 8. Concentrations of liquid and gaseous species versus irradiation time in the presence of selected catalysts during glucose photoreforming.

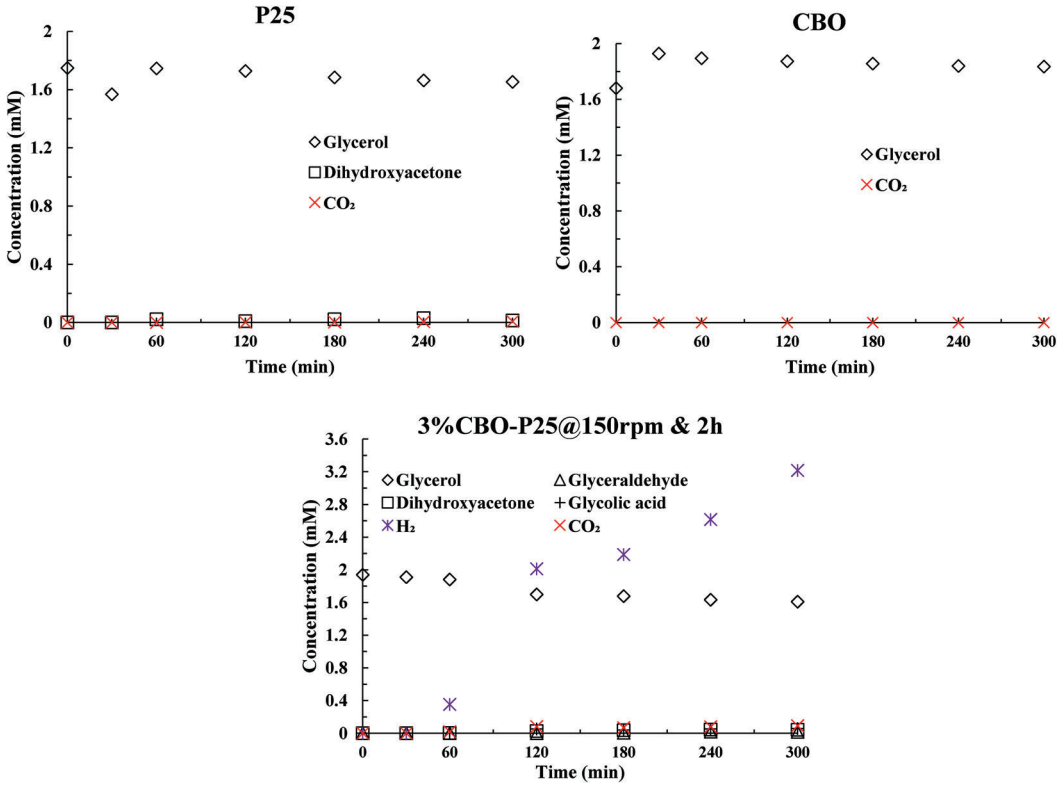

Figure 9. Concentrations of liquid and gaseous species versus irradiation time in the presence of selected catalysts during glycerol photoreforming.

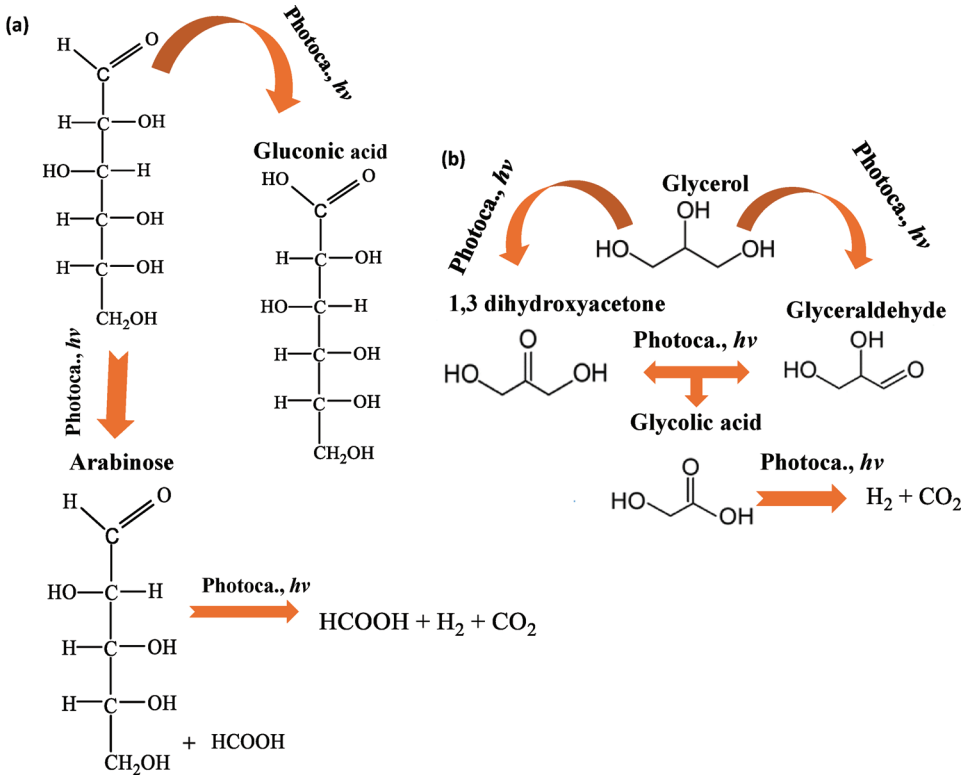

Figure 10. Hypothesized reaction routes of a) glucose and b) glycerol.

4. Conclusions

MBi_2O_4-P25 coupled samples with M (Cu, Ni, Zn, Co) were successfully synthesized by a simple mechanical ball milling. The photocatalytic performance under simulated solar irradiation towards the production of H_2 and the partial oxidation of glycerol and glucose improved compared to unmixed solids. The enhanced photocatalytic activity was attributed to the improved absorption of visible light, the efficient separation of photogenerated electrons and holes and their rapid transmission to the reacting species due to the formation of an effective heterostructure. The most efficient catalyst was 3%CBO-P25@150 rpm & 2 h with a glucose conversion of 34% and H_2 production of 2.6×10^{-3} M. Moreover, arabinose and formic acid were the main products with selectivity values of 57% and 32% respectively. During glycerol photoreforming, a good H_2 production, similar to literature results related to Pt-P25 and different Pt-TiO_2 photocatalysts,[24,36] with the contemporary production of high added value compounds, has been obtained using the composite sample 3%CBO-P25@150 rpm & 2 h.

This study suggests the possibility of replacing noble metals using a simple and easily applicable method in terms of scale-up for the preparation of active photocatalysts not only to produce H_2, but also co-products with high added value.

Conflict of Interest

The authors declare no conflict of interest.

Data Availability Statement

Research data are not shared.

Keywords

biomass photoreforming, H_2 production, heterogeneous photocatalysis, high added value chemicals, spinel/TiO_2 composites

Received: May 2, 2024
Revised: June 3, 2024
Published online: June 16, 2024

[1] K. Srirangan, L. Akawi, M. Moo-Young, C. P. Chou, *Appl. Energy* **2012**, *100*, 172.
[2] M. F. Demirbas, M. Balat, H. Balat, *Energy Convers. Manage.* **2009**, *50*, 1746.
[3] S. Yana, M. Nizar, Irhamni, D. M., *Renewable Sustainable Energy Rev.* **2022**, *160*, 112268.
[4] I. P. Jain, *Int. J. Hydrogen Energy* **2009**, *34*, 7368.
[5] K. Mazloomi, C. Gomes, *Renewable Sustainable Energy Rev.* **2012**, *16*, 3024.
[6] J. Nowotny, T. N. Veziroglu, *Int. J. Hydrogen Energy* **2011**, *36*, 13218.
[7] M. Bellardita, V. Loddo, L. Palmisano, *Mini-Rev. Org. Chem.* **2020**, *17*, 884.
[8] M. A. Al-Nuaim, A. A. Alwasiti, Z. Y. Shnain, *Chem. Pap.* **2022**, *77*, 677.
[9] K. C. Christoforidis, P. Fornasiero, *ChemCatChem* **2017**, *9*, 1523.
[10] M. Bellardita, V. Loddo, V. Augugliaro, L. Palmisano, S. Yurdakal, *Catal. Today* **2024**, *432*, 114587.

[11] M. Yasuda, T. Matsumoto, T. Yamashita, *Renewable Sustainable Energy Rev.* **2018**, *81*, 1627.
[12] H. Zhao, J. Liu, N. Zhong, S. Larter, Y. Li, M. G. Kibria, B. L. Su, Z. Chen, J. Hu, *Adv. Energy Mater.* **2023**, *13*, 2300257.
[13] M. Bellardita, M. Feilizadeh, R. Fiorenza, S. Scirè, L. Palmisano, V. Loddo, *Photochem. Photobiol. Sci.* **2022**, *21*, 2139.
[14] M. Umair, G. Palmisano, R. Al Sakkaf, S. Al Jitan, A. Pintar, G. Žerjav, L. Palmisano, V. Loddo, M. Bellardita, *Appl. Surf. Sci* **2024**, *648*, 159030.
[15] X. Wu, N. Luo, S. Xie, H. Zhang, Q. Zhang, F. Wang, Y. Wang, *Chem. Soc. Rev.* **2020**, *49*, 6198.
[16] A. M. Djaballah, M. Bellardita, L. Palmisano, V. Loddo, M. Umair, C. M. Pecoraro, R. Bagtache, M. Trari, *Mol. Catal.* **2023**, *546*, 113251.
[17] C. Li, H. Wang, S. B. Naghadeh, J. Z. Zhang, P. Fang, *Appl. Catal., B* **2018**, *227*, 229.
[18] L. Llatance-Guevara, N. E. Flores, G. O. Barrionuevo, J. L. Mullo Casillas, *Catalysts* **2022**, *12*, 1091.
[19] M. Bellardita, D. Virtù, F. di Franco, V. Loddo, L. Palmisano, M. Santamaria, *Chem. Eng. J.* **2022**, *431*, 134131.
[20] M. Bellardita, E. I. García-López, G. Marcì, L. Palmisano, *Int. J. Hydrogen Energy* **2016**, *41*, 5934.
[21] J. C. Colmenares, A. Magdziarz, A. Bielejewska, *Bioresour. Technol.* **2011**, *102*, 11254.
[22] J. Kaur, A. K. Sarma, M. K. Jha, P. Gera, *Biotechnol. Rep.* **2020**, *27*, e00487.
[23] V. Maurino, A. Bedini, M. Minella, F. Rubertelli, E. Pelizzetti, C. Minero, *J. Adv. Oxid. Technol.* **2008**, *11*, 184.
[24] C. M. Pecoraro, L. Mino, E. Kozyr, L. Palmisano, F. di Franco, V. Loddo, M. Santamaria, M. Bellardita, *Chem. Commun.* **2024**, *60*, 3782.
[25] D. Chen, J. Liu, X. Qiu, B. Liu, X. Wang, Z. Qiu, X. Lin, Y. Qin, *AIChE J.* **2024**, *70*, 18323.
[26] X. Lin, J. Liu, X. Qiu, B. Liu, X. Wang, L. Chen, Y. Qin, *Angew. Chem., Int. Ed.* **2023**, *62*, e202306333.
[27] S. Çetinkaya, S. Yurdakal, *Catal. Today* **2021**, *380*, 237.
[28] R. Du, C. Wang, L. Guo, R. A. Soomro, B. Xu, C. Yang, F. Fu, D. Wang, *Small* **2023**, *19*, 2302330.
[29] F. Parrino, M. Bellardita, E. I. García-López, G. Marcì, V. Loddo, L. Palmisano, *ACS Catal.* **2018**, *8*, 11191.
[30] C. Prasad, H. Tang, Q. Q. Liu, S. Zulfiqar, S. Shah, I. Bahadur, *J. Mol. Liq.* **2019**, *289*, 111114.
[31] L. Mohapatra, K. M. Parida, K. Parida, *J. Mater. Chem. A* **2016**, *4*, 10744.
[32] B. di Credico, M. Redaelli, M. Bellardita, M. Calamante, C. Cepek, E. Cobani, M. D'arienzo, C. Evangelisti, M. Marelli, M. Moret, L. Palmisano, R. Scotti, *Catalysts* **2018**, *8*, 353.
[33] H. Sun, X. Guo, A. Facchetti, *Chem* **2020**, *6*, 1310.
[34] E. Grabowska, *Appl. Catal., B* **2016**, *186*, 97.
[35] R. Fiorenza, M. Bellardita, S. A. Balsamo, L. Spitaleri, A. Gulino, M. Condorelli, L. D'Urso, S. Scirè, L. Palmisano, *Chem. Eng. J.* **2022**, *428*, 131249.
[36] C. M. Pecoraro, M. Bellardita, V. Loddo, F. Di Franco, L. Palmisano, M. Santamaria, *J. Ind. Eng. Chem.* **2023**, *118*, 247.
[37] R. Fiorenza, M. Bellardita, T. Barakat, S. Scirè, L. Palmisano, *J. Photochem. Photobiol., A* **2018**, *352*, 25.
[38] S. Meng, W. Sun, S. Zhang, X. Zheng, X. Fu, S. Chen, *J. Phys. Chem. C* **2018**, *122*, 26326.
[39] Q. Guo, C. Zhou, Z. Ma, X. Yang, *Adv. Mater.* **2019**, *31*, 1901997.
[40] A. Nikokavoura, C. Trapalis, *Appl. Surf. Sci.* **2017**, *391*, 149.
[41] M. Z. Selcuk, M. S. Boroglu, I. Boz, *React. Kinet., Mech. Catal.* **2012**, *106*, 313.
[42] Z. Jiang, R. Qi, Z. Huang, W. Shangguan, R. J. Wong, A. Lee, *Energy Environ. Mater.* **2020**, *3*, 202.
[43] F. J. López-Tenllado, J. Hidalgo-Carrillo, V. Montes, A. Marinas, F. J. Urbano, J. M. Marinas, L. Ilieva, T. Tabakova, F. Reid, *Catal. Today* **2017**, *280*, 58.
[44] A. M. Djaballah, R. Bagtache, M. Benlembarek, M. Trari, *J. Photochem. Photobiol., A* **2024**, *447*, 115186.
[45] G. Štefanić, S. Krehula, I. Štefanić, *Dalton Trans.* **2015**, *44*, 18870.
[46] M. Muscetta, S. Al Jitan, G. Palmisano, R. Andreozzi, R. Marotta, S. Cimino, I. Di Somma, *J. Environ. Chem. Eng.* **2022**, *10*, 107735.
[47] F. E. Oropeza, N. Y. Dzade, A. Pons-Martí, Z. Yang, K. H. L. Zhang, N. H. De Leeuw, E. J. M. Hensen, J. P. Hofmann, *J. Phys. Chem. C* **2020**, *124*, 22416.
[48] F. Wang, H. Yang, Y. Zhang, *Mater. Sci. Semicond. Process.* **2018**, *73*, 58.
[49] X. Zhu, Z. Guan, P. Wang, Q. Zhang, Y. Dai, B. Huang, *Chin. J. Catal.* **2018**, *39*, 1704.
[50] C. Jagadeesh, P. Suresh, B. B. V. Sailaja, *Int. J. Curr. Adv. Res.* **2017**, *6*, 8605.
[51] M. Bellardita, V. Augugliaro, V. Loddo, B. Megna, G. Palmisano, L. Palmisano, M. A. Puma, *Appl. Catal., A* **2012**, *441-442*, 79.
[52] S. Yurdakal, C. Garlisi, L. Özcan, M. Bellardita, G. Palmisano, in *Heterogeneous Photocatalysis*, Editors Giuseppe Marcì and Leonardo Palmisano, Elsevier, Amsterdam **2019**, pp. 87–152.
[53] F. X. Zhang, S. K. Saxena, *Appl. Phys. Lett.* **2006**, *88*, 141926.
[54] Z. V. Popović, G. Kliche, M. Cardona, R. Liu, *Phys. Rev. B* **1990**, *41*, 3824.
[55] R. Fiorenza, M. Bellardita, S. Scirè, L. Palmisano, *Catal. Today* **2019**, *321–322*, 113.
[56] C. Deiana, E. Fois, S. Coluccia, G. Martra, *J. Phys. Chem. C* **2010**, *114*, 21531.
[57] L. Mino, G. Spoto, S. Bordiga, A. Zecchina, *J. Phys. Chem. C* **2012**, *116*, 17008.
[58] R. Nakamura, A. Imanishi, K. Murakoshi, Y. Nakato, *J. Am. Chem. Soc.* **2003**, *125*, 7443.
[59] P. Praveen, G. Viruthagiri, S. Mugundan, N. Shanmugam, *Spectrochim. Acta, Part A* **2014**, *117*, 622.
[60] J. Huo, Y. Hu, H. Jiang, C. Li, *Nanoscale* **2014**, *6*, 9078.
[61] J. Jiao, Y. Wei, Z. Zhao, J. Liu, J. Li, A. Duan, G. Jiang, *Ind. Eng. Chem. Res.* **2014**, *53*, 17345.
[62] M. E. Aguirre, R. Zhou, A. J. Eugene, M. I. Guzman, M. A. Grela, *Appl. Catal., B* **2017**, *217*, 485.
[63] T. Wei, Y. N. Zhu, X. An, L. M. Liu, X. Cao, H. Liu, J. Qu, *ACS Catal.* **2019**, *9*, 8346.
[64] S. Wang, D. Wang, B. Tian, X. Gao, L. Han, Y. Zhong, S. Song, Z. Wang, Y. Li, J. Gui, M. G. Sendeku, Y. Zhang, Y. Kuang, X. Sun, *Sci. China Mater.* **2023**, *66*, 1801.
[65] M. Bellardita, A. Di Paola, E. García-López, V. Loddo, G. Marcì, L. Palmisano, *Curr. Org. Chem.* **2013**, *17*, 2440.
[66] R. Chong, J. Li, Y. Ma, B. Zhang, H. Han, C. Li, *J. Catal.* **2014**, *314*, 101.
[67] R. Chong, J. Li, X. Zhou, Y. Ma, J. Yang, L. Huang, H. Han, F. Zhang, C. Li, *Chem. Commun* **2014**, *50*, 165.